JCB Journal of Cell Biology

ARTICLE

Bidirectional intraflagellar transport is restricted to two sets of microtubule doublets in the trypanosome flagellum

Eloïse Bertiaux[1,2*], Adeline Mallet[1,2,3*], Cécile Fort[1,2], Thierry Blisnick[1], Serge Bonnefoy[1], Jamin Jung[1], Moara Lemos[1], Sergio Marco[4,5], Sue Vaughan[6], Sylvain Trépout[4,5], Jean-Yves Tinevez[7,8], and Philippe Bastin[1]

Intraflagellar transport (IFT) is the rapid bidirectional movement of large protein complexes driven by kinesin and dynein motors along microtubule doublets of cilia and flagella. In this study, we used a combination of high-resolution electron and light microscopy to investigate how and where these IFT trains move within the flagellum of the protist *Trypanosoma brucei*. Focused ion beam scanning electron microscopy (FIB-SEM) analysis of trypanosomes showed that trains are found almost exclusively along two sets of doublets (3–4 and 7–8) and distribute in two categories according to their length. High-resolution live imaging of cells expressing mNeonGreen::IFT81 or GFP::IFT52 revealed for the first time IFT trafficking on two parallel lines within the flagellum. Anterograde and retrograde IFT occurs on each of these lines. At the distal end, a large individual anterograde IFT train is converted in several smaller retrograde trains in the space of 3–4 s while remaining on the same side of the axoneme.

Introduction

Intraflagellar transport (IFT) is the movement of molecular motors and multiprotein complexes that carry tubulin and other flagellar components to the tip of cilia and flagella for assembly (Kozminski et al., 1993; Craft et al., 2015). One or more kinesin motors are responsible for anterograde transport, whereas a dynein motor returns the trains to the base during retrograde transport (Prevo et al., 2017). These moving protein complexes have been termed IFT trains (Pigino et al., 2009). Absence of IFT prevents construction of most cilia and flagella, whereas perturbation of IFT components can impact on the structure and function of the organelle as observed in multiple human genetic diseases (Beales et al., 2007; Dagoneau et al., 2009; Perrault et al., 2012; Halbritter et al., 2013).

Quantification of IFT in animal cells, green algae, trypanosomes, or ciliates revealed a remarkably high speed (0.5–5 µm/s) and frequency (~1–3 trains/s) of IFT trains in both directions (Iomini et al., 2001; Snow et al., 2004; Besschetnova et al., 2010; Brooks and Wallingford, 2012; Buisson et al., 2013; Williams et al., 2014; Prevo et al., 2015; Wheeler et al., 2015; Wingfield et al., 2017). When anterograde trains reach the distal end, they are converted in usually smaller retrograde trains in the space of a few seconds (Buisson et al., 2013; Chien et al., 2017; Mijalkovic et al., 2017). Trains are fairly large complexes of >20 proteins (Taschner and Lorentzen, 2016) associated to molecular motors whose size is >1 mD (Rompolas et al., 2007), raising the question of how they are organized within the flagellum during anterograde and retrograde trafficking.

In transmission EM (TEM), trains appear as electron-dense particles sandwiched between microtubule doublets and the flagellum membrane. This has been visualized in only two species so far: the green algae *Chlamydomonas reinhardtii* (Ringo, 1967; Pigino et al., 2009; Vannuccini et al., 2016) and the protist *Trypanosoma brucei* (Absalon et al., 2008). Recently, an elegant study using correlative light EM in *Chlamydomonas* cells expressing a fluorescent IFT protein showed that anterograde trains are positioned on the B tubule of each microtubule doublet, whereas retrograde trains are found on the A tubule (Stepanek and Pigino, 2016). In this organism, IFT trains appeared on all nine microtubule doublets (Stepanek and Pigino, 2016). By contrast, TEM suggested that electron-dense particles looking like

[1]Trypanosome Cell Biology Unit, INSERM U1201, Institut Pasteur, Paris, France; [2]Université Pierre et Marie Curie Paris 6, Cellule Pasteur, Paris, France; [3]UtechS Ultrastructural Bioimaging (Ultrapole), Institut Pasteur, Paris, France; [4]Université Paris Sud, Université Paris-Saclay, Centre National de la Recherche Scientifique, UMR 9187, Orsay, France; [5]Institut Curie, Paris Sciences et Lettres Research University, INSERM U1196, Orsay, France; [6]Department of Biological and Medical Sciences, Faculty of Health and Life Science, Oxford Brookes University, Oxford, UK; [7]UtechS Photonic Bioimaging (Imagopole), Institut Pasteur, Paris, France; [8]Image Analysis Hub, Institut Pasteur, Paris, France.

*E. Bertiaux and A. Mallet contributed equally to this paper; Correspondence to Philippe Bastin: pbastin@pasteur.fr.

https://doi.org/10.1083/jcb.201805030

IFT trains are restricted to microtubule doublets 3–4 and 7–8 of the axoneme in *T. brucei* (Fig. 1 A; Absalon et al., 2008; Höög et al., 2016). The restricted presence of IFT trains on two sets of doublets raises two hypotheses. First, a tantalizing explanation would be that some specific doublets serve as tracks for anterograde transport and others for retrograde trafficking, hence allowing independent control of each mode of transport (Fig. 1 B, Model 1). Second, each individual doublet could serve as a double track for IFT (Fig. 1 B, Model 2) as shown in *Chlamydomonas*. In that situation, train frequency and speed could be similar or different between doublets. In both models, once anterograde trains reach the distal end of the flagellum, they need to be converted to retrograde trains in order to return back to the proximal end. Does conversion happen on the same doublet that the anterograde train traveled along, or does each anterograde train enter a common pool of material at the distal end of the flagellum, where retrograde trains are then assembled? In this study, we investigated IFT train distribution along the length of the trypanosome flagellum using focused ion beam scanning EM (FIB-SEM) to get a 3D view and to measure the length of each IFT train using a 10-nm Z axis increment. We formally demonstrate that trains are indeed mostly found on doublets 3–4 and 7–8 and that they fall in two categories defined by their length. Using high-resolution live-cell imaging, we reveal which hypothesis is correct for the distribution of anterograde and retrograde trafficking, and we apply kymograph analysis to examine the conversion of anterograde to retrograde trains.

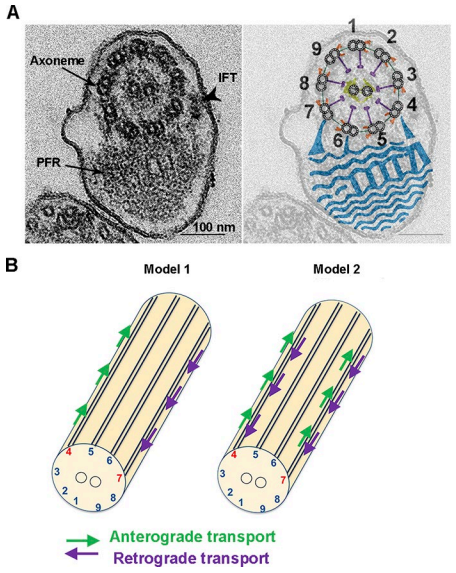

Figure 1. **Positioning of IFT trains in the trypanosome flagellum and models for IFT trafficking. (A)** Cross section of the trypanosome flagellum observed by conventional TEM. The arrowhead indicates an IFT particle positioned at the level of doublet 4. The cartoon shows the main structural components of the axoneme, with the numbering of microtubule doublets (Branche et al., 2006) superposed on the original image. Doublet numbering follows the conventional rules: a line perpendicular to the middle axis of the central pair microtubules is drawn and makes contact with the A tubule of only one doublet that is defined as number 1. The numbering follows the clockwise orientation defined by the dynein arms. Dynein arms are shown in orange, radial spoke in violet, central pair projections in yellow, and the PFR in blue. **(B)** The restricted presence of IFT on doublets 3–4 and 7–8 can be explained by two models: either some doublets are used specifically for anterograde transport and the other ones support retrograde IFT (Model 1) or bidirectional trafficking takes place on all doublets (Model 2). Only one doublet was highlighted for the sake of clarity.

Results

FIB-SEM analysis revealed the length and 3D distribution of IFT trains

To obtain a global view of the 3D distribution of IFT trains by EM, different approaches are available. Since the twisted shape of the trypanosome flagellum (Sherwin and Gull, 1989) restricts the use of conventional transmission electron tomography to short portions of the axoneme, we turned to FIB-SEM, which allows the collection of hundreds of sequential EM images at 10 nm Z resolution (Kizilyaprak et al., 2014). WT trypanosomes were chemically fixed, dehydrated, and embedded in resin in conditions similar to classic TEM. Acquisition in x–y relies on scanning EM collecting backscattered electrons and therefore provides a lower resolution compared with TEM. However, invaluable Z information is gained by milling the block face with 10-nm increments using the ion beam. In these conditions, isotropic large volumes can be acquired with ultrastructural resolution at 10 nm voxel size to analyze intracellular structures in long portions of flagella. This turned out to be a considerable advantage to monitor IFT train positioning. Four samples were reconstructed, each containing several trypanosomes. Navigating through the volume of each sample revealed the typical trypanosome architecture with the cell body containing the subpellicular microtubules, the nucleus, the large mitochondrion and its kinetoplast (mitochondrial DNA), the ER, the Golgi apparatus, or the glycosomes (Fig. 2 A and Video 1). The shape, size, and distribution of these organelles were in agreement with published data based on electron tomography (Lacomble et al., 2009) or serial block face sectioning (Hughes et al., 2017). Flagella were clearly recognized in both cross and longitudinal sections, including multiple cases where the proximal portion was seen to emerge from the flagellar pocket (Video 1). The base of the flagellum displayed the typical organization with the basal body, the transition zone, the axoneme, and finally, the axoneme and the paraflagellar rod (PFR), a lattice-like structure (Hughes et al., 2012) essential for motility (Bastin et al., 1998). Flagella were correctly attached to the cell body with the exception of the distal end, which is always free as expected (Sherwin and Gull, 1989).

Importantly, IFT trains can be seen without ambiguity as electron-dense particles found between the flagellar membrane and microtubule doublets (Fig. 2 A, arrows in bottom panels, and Video 1). To determine doublet number, the fixed orientation of the axoneme relative to the PFR (Branche et al., 2006; Gadelha et al., 2006; Ralston et al., 2006) was exploited (Fig. 1 A). Indeed, the presence of a thick projection that connects the B tubule of doublet 7 to the PFR makes doublet numbering straightforward (Fig. 1 A). In case this projection was not visible, the proximal-to-distal orientation of the axoneme was determined by traveling through the volume knowing that dynein arms are orientated clockwise when starting from the base of the flagellum (Sherwin and Gull, 1989). Because several portions of flagella

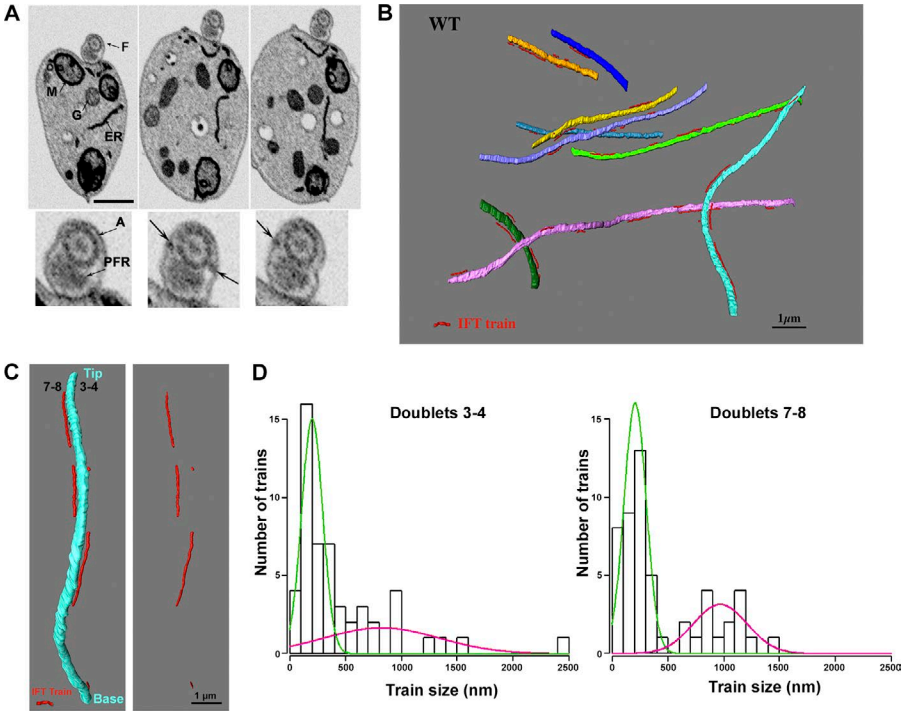

Figure 2. **IFT trains of similar length are distributed on doublets 3–4 and 7–8. (A)** Successive images from Video 1 showing WT trypanosomes analyzed by FIB-SEM. Each image corresponds with a Z stack of three slices between positions 424 and 475. The progression is from anterior to posterior. Top: Low magnification of the cell body with major organelles indicated. F, flagellum; G, glycosome; M, mitochondrion. Bottom: A magnification of the flagellum area is shown with the axoneme (A) and the PFR. The arrows indicate IFT particles. **(B)** Portions of flagella reconstructed after FIB-SEM. Each axoneme is shown with a different color, and IFT trains are in red (for animation, see Video 2). **(C)** Another example of a flagellum from a WT trypanosome coming from a different stack than the one presented in A and B with the axoneme (sky blue) and several IFT trains (red). Doublet numbers and flagellum orientation (basal body and tip) are indicated. **(D)** Length of the IFT trains on doublets 3–4 (green; $n = 52$) and 7–8 (magenta; $n = 56$) determined from FIB-SEM analysis. Data are from 27 portions of flagella representing a total axoneme length of 166 µm. Two populations can be separated with short trains (green) and longer ones (magenta; see text for details).

were encountered in a single volume, each axoneme was individually marked with a different color, and IFT trains are indicated in red (Fig. 2, B and C; and Video 2). Most trains were found along doublets 3–4 and 7–8 and exhibited various lengths (Fig. 2, B and C). We detected 52 trains closely associated to doublets 3–4 and 56 trains to doublets 7–8 in 27 distinct flagella (total cumulated axoneme length was 166 µm, and the average length of the visible axoneme was 6.25 ± 4.21 µm). Only two trains were not found on these doublets (both were present on doublet 1). All of the reconstructed axonemes from the FIB-SEM data were pooled in order to calculate an average train number in a typical axoneme. An average of 6.15 trains were found associated to doublets 3–4, and 6.6 trains on doublets 7–8. This is below the expected numbers of 8.6 anterograde trains and 8.9 retrograde trains per flagellum deduced from their speed and frequency in live cells (Buisson et al., 2013), suggesting that some trains might be missed in the FIB-SEM analysis.

Measurements of the length of IFT trains from the FIB-SEM data suggested the presence of two distinct populations on each set of doublets (Fig. 2 D). This was confirmed by statistical analysis using R software, with 61% short trains (202 ± 94 nm) and 39% longer trains (822 ± 515 nm) associated to doublets 3–4 ($n = 52$), whereas 68% short trains (207 ± 99 nm) and 32% longer trains (968 ± 239 nm) associated to doublets 7–8 ($n = 56$; Fig. 2 D).

In most cases, the random orientation of flagella restricted the discrimination of individual doublets in the FIB-SEM volumes. However, we could find a few flagella whose positioning allowed the segmentation of individual doublets, hence offering the opportunity to see whether IFT trains associated preferentially to doublet 3 or 4 or to doublet 7 or 8. One such example is presented in Fig. 3 and corresponds with the cell in the center of the field of view in Video 1. Doublets could be segmented over several micrometers, and four trains were present along them. Trains annotated as IFT1, IFT2, and IFT4 were all found to be in closer proximity to doublet 7 compared with doublet 8, whereas train IFT3 was closer to doublet 4 than to doublet 3 (Fig. 3). This suggests that IFT trains could travel mostly on doublets 4 and 7. Unfortunately, this analysis was only feasible with very few flagella and cannot be taken as a generality.

Overall, these results demonstrate that IFT trains are restricted to doublets 3–4 and 7–8 along the length of the flagellum in trypanosomes, with a possible preference for 4 and 7 at least in some flagella. The average train number and their average length are equivalent for the two sets of doublets, hence suggesting that similar trains travel on each of them rather than supporting the second hypothesis of anterograde and retrograde IFT trafficking taking place on each doublet. However, FIB-SEM does not give information on train direction, and the possible presence of arrested trains (Stepanek and Pigino, 2016) cannot be ruled out and could interfere with the interpretation. Now that the spatial distribution of IFT trains has been clarified, we turned to live-cell imaging in order to investigate their dynamics.

Immunofluorescence analysis indicates that IFT proteins are found on both sides of the axoneme

Measurements of flagellar sections by TEM showed that the doublets 4 and 7 are separated by 190 ± 11 nm ($n = 20$), which is below the resolution of conventional light microscopy. To evaluate the feasibility of detecting IFT on these two separate sides of the axoneme, we tried different fixation protocols and examined the distribution of IFT proteins by immunofluorescence assays with antibodies against the IFT172 protein (Absalon et al., 2008) and the axonemal protein TbSAXO1 (Dacheux et al., 2012). Fixation of trypanosomes in paraformaldehyde followed by a postfixation in methanol led to the detection of TbSAXO1 as a single thick line (second column, Fig. 4) as expected from immunogold analysis

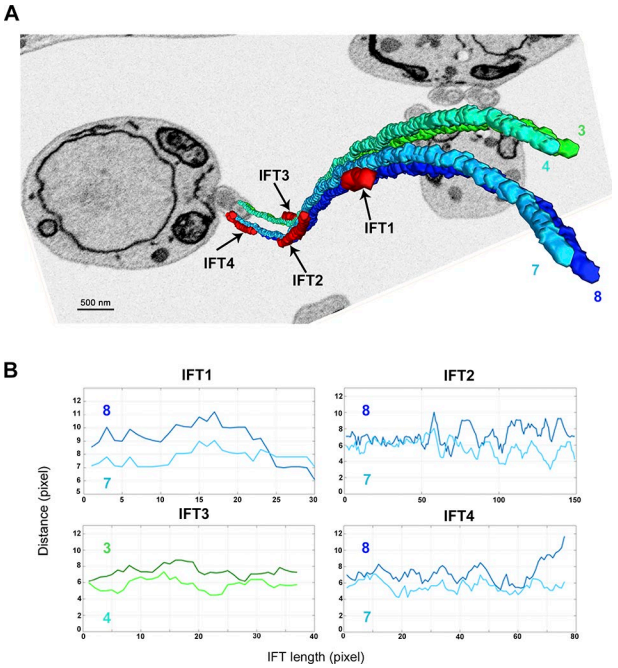

Figure 3. **IFT trains are found closer to doublets 4 and 7 compared with doublets 3 and 8. (A)** 3D view of a rare flagellum where individual doublets could be discriminated. Segmentation was performed to highlight the vicinity of the IFT trains (red) and microtubule doublets 3 (dark green), 4 (light green), 7 (light blue), and 8 (dark blue). **(B)** Plots representing the distances between the center of the skeleton for the indicated IFT trains and that of the microtubule doublets along their length using the same color code. In this flagellum, IFT trains are found closer to doublets 4 and 7.

that showed that this protein was present throughout the axoneme (Dacheux et al., 2012). By contrast, IFT172 staining appeared as two parallel lines decorating both sides of the TbSAXO1 staining (third column, Fig. 4). This was observed in the single flagellum of G1 cells (Fig. 4 A) and in both mature and growing flagella of duplicating cells (Fig. 4 B). Methanol fixation results in dehydration and flattens the sample on the slide, possibly leading to a better separation of IFT trains allowing their detection as two separate lines by conventional light microscopy. This is promising because this suggests that IFT positioning on distinct doublets could be discriminated by light microscopy.

The next step was the investigation of IFT in live cells, which requires the expression of a fluorescent reporter in trypanosomes (Adhiambo et al., 2009; Bhogaraju et al., 2013; Buisson et al., 2013; Huet et al., 2014). Cell lines expressing GFP::IFT52 have been used reproducibly to detect IFT (Absalon et al., 2008; Buisson et al., 2013), but in this setup, GFP::IFT52 was expressed from the ribosomal DNA locus with a strong promoter (Wirtz and Clayton, 1995). This led to bright flagellar signal but also to significant cytoplasmic signal (Buisson et al., 2013). To avoid any risk of potential artifacts due to overexpression, an in situ tagging approach (Kelly et al., 2007; Dean et al., 2017) was selected to generate a cell line expressing IFT81 fused to mNeonGreen (mNG; Shaner et al., 2013) from its endogenous locus. IFT81 is a well-known member of the IFT-B complex involved in tubulin binding and transport (Bhogaraju et al., 2013; Kubo et al., 2016) and was shown previously to traffic within the trypanosome flagellum (Bhogaraju et al., 2013). Western blotting with an anti-mNG antibody demonstrated that the fusion protein displayed the expected mobility on SDS-PAGE (Fig. S1 A). Live analysis showed the classic distribution with a strong signal at the base of the flagellum and train trafficking in both anterograde and retrograde direction within the flagellum that was detected by kymograph analysis (Fig. S1, B and C; and Video 3). Kymograph analysis revealed that the frequency and speed of anterograde trains (Fig. S1, D and E) was similar to what was reported previously for other IFT-B proteins (Bhogaraju et al., 2013; Buisson et al., 2013; Huet et al., 2014). Finally, applying the paraformaldehyde–methanol fixation protocol followed by direct observation of the mNG::IFT81 fluorescent signal led to the detection of two parallel lines within flagella (Fig. S1 F). The behavior of mNG::IFT81 is therefore comparable with that of GFP::IFT52, and both cell lines were used for imaging IFT in trypanosomes.

High-resolution live-cell imaging reveals bidirectional IFT on two sides of the axoneme

These results are encouraging because they suggest that live imaging by light microscopy could permit the visualization of IFT on two sides of the axoneme. We turned to superresolution based on structured illumination microscopy (SIM; Gustafsson, 2000; Gustafsson et al., 2008) to visualize IFT trafficking. SIM imaging provided the spatial resolution and demonstrated the

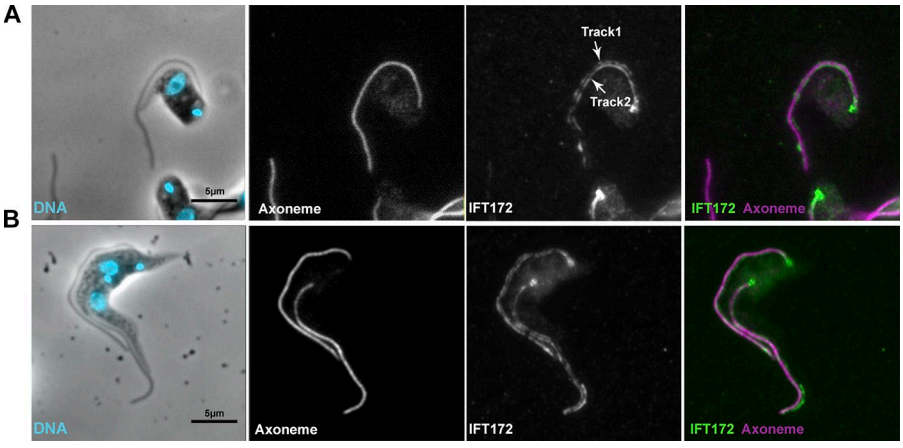

Figure 4. **IFT proteins are found on two distinct lines along the axoneme in fixed cells. (A and B)** Control trypanosomes (strain expressing YFP::ODA8; Bonnefoy et al., 2018) were fixed in paraformaldehyde followed by methanol after fixation and processed for immunofluorescence using a marker antibody for the axoneme (middle; magenta on the merged image) and a monoclonal antibody against IFT172 (right; green on the merged image). The leftmost panel shows the phase-contrast image merged with DAPI staining (cyan). **(A)** Cell with one flagellum. **(B)** Cell assembling a new flagellum. In both cases, a single continuous thick line was observed for the axoneme marker, whereas discontinuous staining spreading on two close but distinct lines was visible for IFT172.

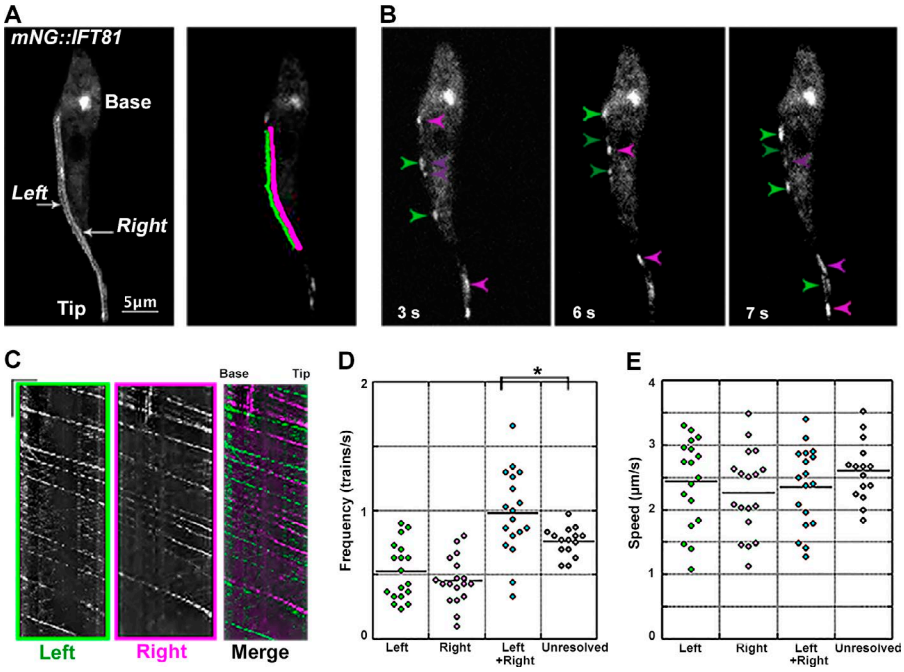

Figure 5. **Bidirectional IFT trafficking takes place on two sides of the axoneme in live trypanosomes expressing mNG::IFT81. (A)** Temporal projection of a stack of images corresponding with Video 5 showing the presence of two parallel lines for IFT in the flagellum in addition to the pool of IFT at the base. The left (green) and right (magenta) sides were defined after orientating the cell with the posterior end on top of the image and the flagellum on the left-hand side. **(B)** Still images from Video 5 of live trypanosomes expressing mNG::IFT81 imaged at high resolution. Green and magenta arrowheads indicate trains on the left and right sides, with light arrowheads indicating anterograde trains and darker arrowheads showing retrograde trains. The time point for each image is indicated. **(C)** Kymograph analysis of the same cell showing trafficking on the left side (green), on the right side (magenta), and the merged images for the region of interest indicated in A. Bars: 2.5 µm (horizontal bar); 2.5 s (vertical bar). **(D)** Dot plot of the frequency of anterograde IFT trains visible on the left (green) and the right (magenta) side, the sum of both (cyan), and from videos where only one track was visible (unresolved; gray). Values are coming from 18 different cells containing a total of 529 trains. *, P = 0.02. **(E)** Same representation but for the speed of anterograde trains. Only statistically significant differences are shown (one-way ANOVA test).

existence of two parallel lines within the flagellum for fluorescent mNG::IFT81 in live cells (Fig. S2 A). Next, we tried to record IFT trafficking over time using the GFP::IFT52 cell line (Fig. S2 B and Video 4). This demonstrated that IFT trains move on two distinct parallel lines in trypanosomes in agreement with the EM data. However, the acquisition time (800 ms) was not compatible with the rapid speed of IFT in trypanosomes (~2 µm/s for anterograde and ~5 µm/s for retrograde transport), and images of multiple trains overlapped, precluding analysis (Video 4).

To find an appropriate compromise between sufficient resolution and fast acquisition, high-resolution imaging was performed using objectives with superior NA (1.49 NA for GFP::IFT52 [imaging performed at the Janelia Farm Research Campus], and 1.57 NA for mNG::IFT81 [imaging performed at the Institut Pasteur]; Li et al., 2015). In these conditions, the theoretical resolution for a green fluorescent molecule should be ~160 nm, a value compatible with the discrimination of IFT trafficking on doublets separated by 190 nm. Remarkably, examination of cells expressing mNG::IFT81 (Video 5) or GFP::IFT52 (Video 6) with the high-NA objectives revealed the presence of trains on two parallel lines within the flagellum. This was clearly confirmed with time projections (Figs. 5 A and S3 A). Closer examination of IFT trafficking demonstrated that anterograde and retrograde IFT trafficking was taking place on each of these lines (Figs. 5 B and S3 B; and Videos 5 and 6). This was further supported by kymograph analysis that showed the presence of distinct anterograde and retrograde trains on each side of the axoneme (Figs. 5 C and S3 C). These results demonstrate that IFT takes place on two separate tracks in the trypanosome flagellum, presumably corresponding with doublets 3–4 and 7–8, and that anterograde and retrograde trafficking occurs on each of them. This supports the hypothesis of bidirectional IFT on both sets of doublets and probably invalidates the model with one track for each direction. However, we cannot formally exclude that anterograde trafficking takes place on doublet 4 and retrograde on doublet 3 or the opposite, and similarly with doublets 7 and 8.

To be able to quantify and compare IFT train trafficking on each side of the axoneme, it was necessary to find a way to identify them. To do that, the cellular asymmetry of trypanosomes was exploited. Cells were orientated with the posterior end toward the top of the image and with the flagellum lying on the left-hand side, hence defining a left and a right side (Figs. 5 A and S3 A). Quantification of anterograde IFT train trafficking showed a similar frequency close to 0.5 anterograde trains/s on the left and right side for both fluorescent proteins (Figs. 5 D and S3 D; Table 1). There was no statistically significant difference between these two parameters in cells expressing mNG::IFT81 (one-way ANOVA test, P = 0.29) or GFP::IFT52 (P = 0.14). The anterograde speed was ~2.5 µm/s on each side in both cell lines (Figs. 5 E and S3 E; and Table 1), although we noted a trend toward slower IFT speed by 10–15% on the right side (P = 0.20 for mNG::IFT81; P = 0.067 for GFP::IFT52). Trains trafficking simultaneously on each side might not be discriminated with conventional light microscopy. Hence, the anterograde IFT train frequency was compared using videos of mNG::IFT81 cells acquired in the same experiment but where two sides could not be discriminated (Fig. 5 E, Unresolved). The frequency calculated from the total of left and right kymographs in cells where the two sides could be detected was consistently higher (0.98 anterograde trains/s) compared with cells where only one line was visible

(0.76 anterograde trains/s; Table 1) with statistical confidence (P = 0.02). This result suggests that ≥15% of trains could be missed when IFT was imaged at low resolution. By contrast, their average train speed was indistinguishable (Table 1; P = 0.21), suggesting that the "missed" trains are not a specific population at least in terms of speed.

Although retrograde transport was detected in almost all videos (Videos 5 and 6), the lower intensity of these trains made their quantification quite challenging, especially for the frequency. Nevertheless, it was possible to estimate the speed of the brightest retrograde trains, which was between 4 and 5 µm/s, in agreement with data obtained using conventional imaging (Buisson et al., 2013).

Although our live-cell imaging data reveal two separate paths for IFT, we wanted to confirm that the IFT motors that connect IFT particles to microtubules exhibit the same. Molecular motors of the kinesin and dynein family transport IFT proteins in the anterograde and retrograde directions, respectively. We investigated the movement of the dynein motor and monitored its association to the IFT proteins. First, we monitored the movement of dynein using the heavy chain 2.2 (DHC2.2) fused to GFP (Blisnick et al., 2014) using high-resolution imaging. As for IFT52 and IFT81, trafficking on two parallel lines on each side of the axoneme was detected (Fig. 6 A and Video 7; *n* = 14). Kymograph analysis confirmed independent movement in anterograde and retrograde directions on both sides (Fig. 6 B). We next set up dual-color imaging to visualize simultaneously mNG::IFT81 and DHC2.1 tagged in situ with TandemTomato (TdT) in live cells. Overall, both signals seemed to colocalize in moving and standing trains (Fig. 6 C and Video 8). Analysis of 10 cells revealed that 93% and 81% of the anterograde traces were positive for both mNG::IFT81 and TdT::DHC2.1 in the anterograde (*n* = 273 trains) and retrograde (*n* = 41) direction. Lower values for retrograde trains probably reflect the weaker fluorescent signal produced by the TdT::DHC2.1 compared with mNG::IFT81. This shows that dynein motors indeed transport cargoes on a limited set of microtubules. However, the TdT fluorescent protein emits at too high of a wavelength to allow sufficient resolution to discriminate the two sides of the axoneme, making it impossible to formally rule out that dynein could travel alone without cargo on other microtubules in the retrograde direction. The same experiment could not be done with IFT kinesins since tagging disrupted protein localization (not depicted). The hypothesis that IFT kinesins walk without cargo on other doublets than 3–4 and 7–8 therefore remains open.

Conversion of anterograde to retrograde train takes place on the same side of the axoneme

To visualize the conversion of anterograde to retrograde transport, we looked at the distal end of the flagellum of cells expressing mNG::IFT81 (Fig. S4 A and Video 9). On both left and right sides, the arrival of large anterograde trains at the distal end of the flagellum was clearly visible. This was followed by a lag phase (seen as vertical lines on the kymograph), where the fluorescent material remained at the distal end but its intensity progressively went down while multiple retrograde trains were released during a ∼3-4-s period (Fig. S4 B). It should be noted that the anterograde trains do not all stop exactly at the same place (Fig. S4 B, merge). Data suggested that anterograde trains convert to retrograde trains on the same track and that no exchange of IFT-B material could be detected between the left and right sides of the axoneme. However, the high frequency of IFT in both directions and the relatively weak signal of retrograde trains make it difficult to reach a firm conclusion. We therefore used the GFP::IFT52-expressing cell line where the signal is brighter, hence facilitating the detection of retrograde transport. The distal end of the flagellum was bleached, and IFT was recorded in this portion (Fig. 7 and Video 10). This led to a significant improvement of the signal-to-noise ratio and helped the visualization of retrograde trains on videos and on kymographs. The arrival of several anterograde trains and their conversion to retrograde trains was tracked by carefully examining video images and performing kymograph analyses (Fig. 7 and Video 10). We could not see an exchange of sides scrutinizing 12 videos acquired in these conditions, following dozens of trains in each.

Overall, these results obtained with two different cell lines (expression of mNG::IFT81 and GFP::IFT52) at two different imaging centers (Janelia Farm, Ashburn, VA, and Institut Pasteur, Paris, France) using different techniques demonstrate that IFT takes place on two distinct sides of the flagellum and that anterograde and retrograde trafficking occur on each of them.

Table 1. **Speed and frequency of anterograde IFT trafficking**

	Speed (µm/s)	Frequency (trains/s)	*n* trains
mNG::IFT81			
Left	2.43 ± 0.68	0.52 ± 0.22	284
Right	2.27 ± 0.65	0.45 ± 0.18	245
Left + right	2.35 ± 0.62	0.98 ± 0.33	529
Unresolved[a]	2.60 ± 0.46	0.76 ± 0.11	389
GFP::IFT52			
Left	2.56 ± 0.26	0.43 ± 0.10	138
Right	2.18 ± 0.29	0.34 ± 0.17	110
Left + right	2.37 ± 0.26	0.77 ± 0.15	248

Data were obtained from 18 and 10 cells for mNG::IFT81 and GFP::IFT52, respectively.
[a]Corresponds with videos acquired in high-resolution conditions but where only one track could be visualized, presumably due to the orientation of the flagellum during the acquisition. Indeed, doublets 3–4 and 7–8 are on opposing sides of the axoneme. According to the orientation of the flagellum on the slide, they can be parallel to the glass slide, and two tracks are visible. However, if the flagellum is twisted by 90°, the two sets of doublets will be on top of each other and will not be resolved even when using high-resolution conditions.

Discussion

T. brucei is only the second organism where IFT trains have been visualized in both light microscopy and EM. In this study, we reveal train distribution on doublets 3–4 and 7–8 using FIB-SEM (with possibly a preference for 4 and 7) and demonstrate bidirectional trafficking on two separate sides of the axoneme by

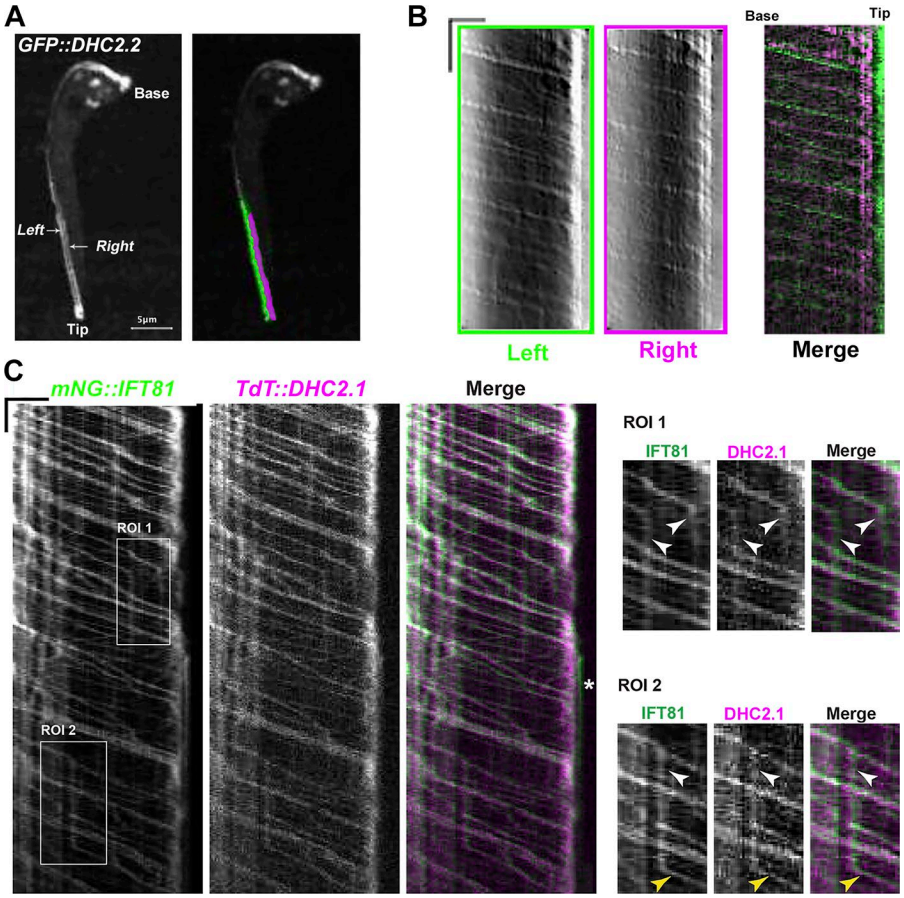

Figure 6. **The IFT dynein travels on both sides of the axoneme in association with IFT proteins. (A)** Temporal projection of the flagellum in a cell expressing GFP::DHC2.2. The region of interest (ROI) at the tip of the flagellum is indicated with left (green) and right (magenta) sides highlighted. **(B)** The kymographs are shown for the left and right side in the corresponding colors. Bars: 2.5 µm (horizontal bar); 5 s (vertical bar). **(C)** Kymograph analysis of a cell expressing mNG::IFT81 (left) and TdT::DHC2.1 (middle). On the merged panels, mNG::IFT81 is shown in green, and TdT::DHC2.1 is in magenta. Both proteins colocalized in moving but also in standing trains shown in the regions of interest. White arrowheads indicate arrested trains, while yellow arrowheads indicate an arrested train that started moving again. Even in these conditions, mNG::IFT81 and TdT::DHC2.1 remained associated. The white asterisk on the merged panel indicates a rare example of mNG::IFT81 material that was not associated with TdT::DHC2.1 and that remained immotile at the far distal end of the flagellum. However, the resolution was not sufficient to rule out the possibility that dynein could travel without cargo on other microtubules.

high-resolution live-cell imaging. These two sides presumably correspond with doublets 3–4 and 7–8, but definitive confirmation will require the identification of specific markers of each of these doublets at the axoneme level.

FIB-SEM detected two distinct populations of trains on each set of doublets. The first possibility is that long trains correspond with anterograde ones and short trains with retrograde ones as expected from the distinctive size on videos and kymographs (Buisson et al., 2013). The higher frequency of short trains (2.3 to 1.5-fold) is consistent with the higher abundance of retrograde trains detected during live imaging (Buisson et al., 2013). However, the total number of IFT trains seen in FIB-SEM (12.5 per flagellum) is lower compared with what was detected by live imaging (17.5). Moreover, the average length of long trains is close to 1 µm, and this is highly unusual for anterograde trains seen on kymographs, in contrast with arrested trains that look larger (Fig. S4). Intriguingly, two populations of IFT trains were also found using electron tomography analysis of *Chlamydomonas* flagella, with average lengths fairly close to what is reported in this study for trypanosomes (Pigino et al., 2009). Long trains were initially thought to correspond with anterograde trains because they accumulate in the *fla14* retrograde transport mutant, where small trains disappear. However, correlative light and electron microscopy (CLEM) revealed that long trains correspond with standing material and that short particles correspond with anterograde trains (Stepanek and Pigino, 2016). Based on this, we propose that short and long trains observed by FIB-SEM in *T. brucei* flagella could correspond with anterograde trains and standing material, respectively. A total of 7.2 short trains was found per flagellum, which is close to the predicted number of 8.6 (Buisson et al., 2013). Observation of kymographs indicated the presence of standing trains that look larger than moving trains (Fig. S4 B, asterisks). It should be noted that this material does not remain stuck forever as it appears to be picked up by other anterograde trains after a few seconds (asterisks in Figs. S1 E and S4 B). In this scenario, retrograde trains would be missed either because they are too short or because their morphology is different and difficult to identify by FIB-SEM. In *Chlamydomonas*, retrograde trains appear less condensed and less regular compared with anterograde trains, and had been missed in conventional TEM until their identification by correlative techniques (Stepanek and Pigino, 2016).

The use of superior NA objectives appears to be an optimal compromise between speed of acquisition and spatial resolution. It revealed the existence of bidirectional IFT on two sides of the axoneme, but it also showed that the frequency of IFT measured with conventional microscopy might be slightly underestimated. Moreover, it revealed the transition of anterograde trains to retrograde trains, with IFT-B proteins spending up to 3–4 s at the distal end while being progressively associated to the emergence of several retrograde trains. This value is in agreement with previous low-resolution analysis based on photobleaching experiments (Buisson et al., 2013). In *Chlamydomonas* (Chien et al., 2017) and *Caenorhabditis elegans* (Mijalkovic et al., 2017), IFT-B

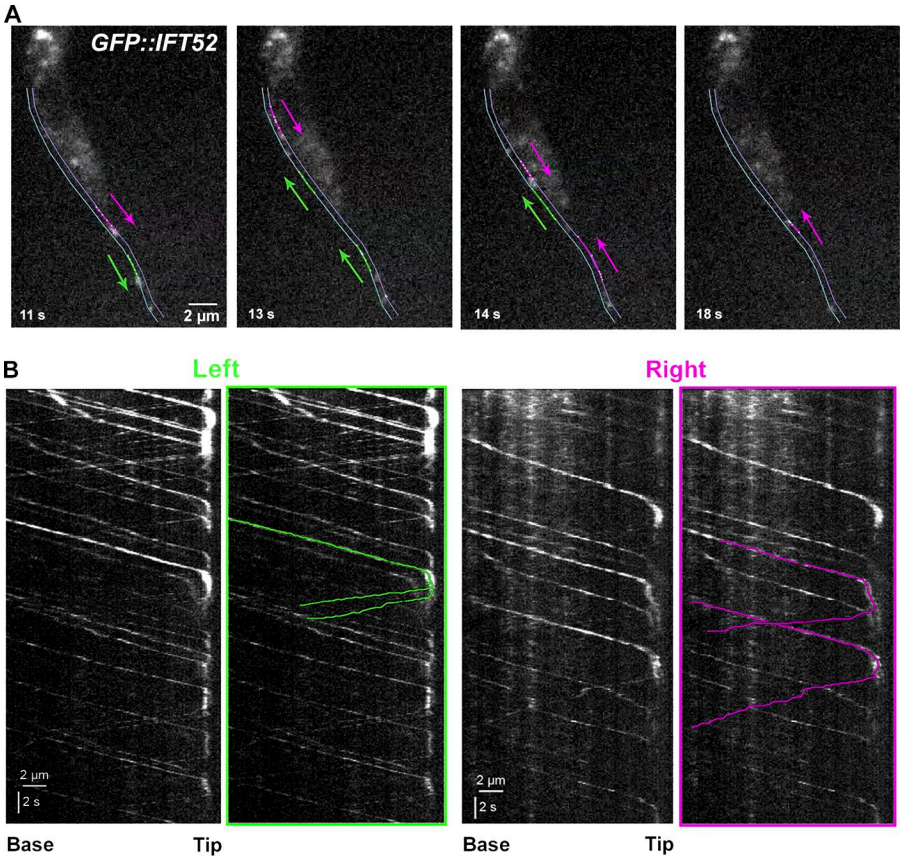

Figure 7. **Anterograde trains are converted to retrograde trains while remaining on the same track. (A and B)** IFT trafficking was analyzed in the GFP::IFT52-expressing cell line. The tip of the flagellum was bleached, and the arrival of new anterograde trains was monitored (see corresponding Video 10). For technical reasons, the bleaching event could not be recorded, and only the recovery phase can be presented. **(A)** Still images corresponding with the indicated times from Video 10. The thin green and magenta lines indicate the left and right sides of the axoneme, respectively. At 11 s, two anterograde trains were marked with a green (left side) or a magenta (right side) line, and the corresponding arrows indicate their direction. At 13 s, the left anterograde train converted to two retrograde ones that remained on the same left side of the flagellum. A second anterograde train arrived on the right side. At 14 s, the first left retrograde train left the field of view, and the second one progressed toward the base of the flagellum. The first anterograde train of the right side converted to a retrograde one that also remained on the right side. At 18 s, all retrograde trains on the left side were not in the field of view anymore as well as the first one on the right side. A new retrograde train was present on the right side and issued from the second anterograde train. Once again, conversion took place on the same side of the axoneme. **(B)** Kymograph analysis for the indicated left and right sides of the flagellum. The original kymograph is shown on the left of each panel, and the three annotated trains described above are marked in color.

proteins also spend a few seconds at the distal end of microtubules before returning toward the base as components of several retrograde trains.

The restriction of IFT to a limited set of doublets is different from the situation encountered in *Chlamydomonas*, where trains appear to be present on the majority of the doublets (Stepanek and Pigino, 2016). So far, IFT trains have only been visualized by EM in these two organisms. To understand the significance of IFT presence on all or only some doublets, it will be essential to determine which doublets are being used in different types of cilia in various organisms. This raises the question of why restrict IFT to some doublets. We propose a scenario where the restriction of IFT to some doublets would represent an evolutionary advantage by liberating the other doublets from constraints imposed by IFT train presence, thereby offering the opportunity for acquiring new structures or functions. In trypanosomes and related protists, the PFR is tightly associated to the axoneme (Koyfman et al., 2011; Hughes et al., 2012) and brings an essential contribution to flagellum motility (Santrich et al., 1997; Bastin et al., 1998). Restricting IFT to some doublets could allow the passage of other molecular motors on the remaining doublets. These could transport different cargoes, hence increasing the range of functions performed by cilia and flagella. In trypanosomes, an unusually large number of genes encoding for kinesins has been identified (Berriman et al., 2005), and several of the protein products have been localized to the flagellum (Demonchy et al., 2009; Chan and Ersfeld, 2010) or found in proteomic analyses of purified flagella (Broadhead et al., 2006; Oberholzer et al., 2011; Subota et al., 2014).

The trypanosome flagellum is attached to the cell body for most of its length toward the PFR side. Doublets 1, 2, 3, 8, and 9 are toward the surface of the flagellum, and the absence of IFT could favor interactions with host tissues. For example, parasites interact with the epithelium of the salivary glands of the tsetse fly via their flagellum and the development of electron-dense material resembling hemidesmosomes (Tetley and Vickerman, 1985). In other organisms, the cilia of sensory neurons of *C. elegans* spring to mind. They are composed of a middle segment made of nine doublet microtubules and of a distal segment with only singlet microtubules. Bidirectional IFT was reported on both segments without collisions (Snow et al., 2004). If some microtubules were used only for anterograde IFT and others only for retrograde IFT, it would provide a way to avoid collisions (Kuhns and Blacque, 2016).

In this study, we show a striking functional difference between doublets 3–4 and 7–8 and the others that cannot sustain IFT. Although microtubule doublets look similar, discrete molecular and structural differences have been noted between them in several organisms (Heuser et al., 2012; Lin et al., 2012). This is also the case in trypanosomes, where doublets 4, 5, 6, and 7 are physically linked to the PFR by different structures (Sherwin and Gull, 1989; Hughes et al., 2012) that could contain unique proteins (Imboden et al., 1995). Other molecular differences between doublets start to be unveiled with the recent example of CFAP43

and CFAP44, two proteins required for motility that have been located to doublets 5 and 6 using superresolution microscopy (Coutton et al., 2018).

What could make doublets 3–4 and 7–8 different from the others, and why would they be used for IFT? One possibility is that they contain biochemical information that is preferentially recognized by the IFT molecular motors once they are associated to the IFT train. Promising candidates are posttranslational modifications of tubulin such as (poly)glycylation or (poly)glutamylation. These are found at the surface of the tubulin dimer, where one would expect interactions with molecular motors (Konno et al., 2012; Sirajuddin et al., 2014). Insights into a potential molecular mechanism are provided by in vitro experiments using engineered tubulin with various posttranslational modifications. This revealed that recruitment and processivity of the IFT kinesin motor KIF17 was stimulated by polyglutamylation (Sirajuddin et al., 2014). Polyglutamylation and polyglycylation are overwhelmingly represented in cilia and flagella, and their alteration affected these organelles (Rogowski et al., 2009; Wloga et al., 2009; Pathak et al., 2011; Lee et al., 2012; Bosch Grau et al., 2013). Mass spectrometry showed that trypanosome tubulin is extensively polyglutamylated, with variable numbers of glutamate residues added to both cytoplasmic and flagellar microtubules (Schneider et al., 1997). Investigating the role of tubulin glutamylation in the definition of microtubule heterogeneity will be an exciting but challenging future axis for research given the large number of enzymes involved in this process (Janke et al., 2005; van Dijk et al., 2007), including in *T. brucei* (Casanova et al., 2015).

Materials and methods

Trypanosome cell lines and cultures

Cell lines used for this work were derivatives of *T. brucei* strain 427 cultured at 27°C in SDM79 medium supplemented with hemin and 10% FCS (Brun and Schönenberger, 1979). Cell lines expressing GFP::DHC2.1 or GFP::DHC2.2 have been described previously (Blisnick et al., 2014). The cell line expressing GFP::IFT52 from the pHD430 vector (Absalon et al., 2008) under the control of the tet repressor (produced by plasmid pHD360; Wirtz and Clayton, 1995) was transformed to express a TdT::IFT81 fusion produced from its endogenous locus (Bhogaraju et al., 2013). For the generation of the mNG::IFT81-expressing cell line, the first 497 nucleotides of *IFT81* (Gene DB number Tb927.10.2640 without the ATG) were chemically synthesized (GeneCust) and cloned in frame with the *mNG* gene (Shaner et al., 2013) within the HindIII and ApaI sites of p2675 vector (Kelly et al., 2007). The construct was linearized within the *IFT81* sequence with the enzyme XcmI and nucleofected (Burkard et al., 2007) in the WT 427 cell line, leading to an integration by homologous recombination in the endogenous locus and to expression of the full-length coding sequence of IFT81 fused to mNG. The same procedure was used for endogenous tagging of the heavy chain DHC2.1 subunit of the dynein motor using the first 497 bp of the coding sequence (Gene DB number Tb927.4.560 without the ATG) cloned in the p2845 vector containing the *TdT* gene and linearized with Csi1. Transfectants were grown in media with the appropriate antibiotic concentration, and clonal populations were obtained by limited dilution.

FIB-SEM

Trypanosomes were fixed directly in medium with 2.5% glutaraldehyde (Sigma-Aldrich), cells were spun down, the supernatant was discarded, and the pellet was incubated for 15 min in fixation buffer made of 2.5% glutaraldehyde and 4% paraformaldehyde in cacodylate 0.1 M buffer, pH 7.4. Samples were washed three times with 0.1 M cacodylate buffer (5 min each) and postfixed with 1% osmium (EMS) and 1.5% potassium ferrocyanide (Sigma-Aldrich) in 0.1 M cacodylate buffer for 1 h. Samples were treated for 30 min with 1% tannic acid (Sigma-Aldrich) and 1 h with 1% osmium tetroxide (EMS), rinsed in water, and dehydrated in an ethanol (Sigma-Aldrich) series of 25%, 50%, 75%, 90%, and 100% (15 min each). Cells were embedded in epoxy resin (EMS) after 48 h at 60°C of polymerization. Embedded samples were mounted on aluminum stubs. Blocks were trimmed with glass knives in such a way that exposure of vertical faces allowed lateral milling by FIB. Tomographic datasets were obtained using a field emission scanning electron microscope (FESEM) Zeiss Auriga microscope equipped with a CrossBeam workstation (ZEISS) and acquired using ATLAS 3D software (ZEISS). For milling with the focused Gallium-ion beam, the conditions were as follows: 0.5–1 nA milling current of the Gallium emitter leading to the removal of 10 nm at a time from the epoxy resin. Scanning EM images were recorded with an aperture of 60 µm in the high-current mode at 1.5 or 2 kV of the in-lens EsB detector with the EsB grid set to −1,000 V. Depending on the respective magnification, voxel size was in a range between 10 and 20 nm in x/y and 10 nm in z. Contrast of the images was inverted to conventional brightfield. Two different people performed the manual annotation of IFT trains. These were defined as electron-dense structures sandwiched between the axoneme and the flagellum membrane and present on a minimum of three consecutive slices (30 nm). Densities associated to membrane distortions were excluded. Trains were defined as different when separated by a minimum of three slices (30 nm).

Data processing and 3D reconstruction

Alignment of image stacks was done with the open source software ImageJ for data alignment (National Institutes of Health; Schneider et al., 2012) and Amira Software for visualization (v6.0.1; FEI; Thermo Fisher Scientific). Segmentation and 3D reconstructions were performed semiautomatically using Amira software and were corrected manually.

Length measurement of IFT trains

Segmentations of flagella and IFT trains were first split according to their segmented colors and then skeletonized in ImageJ (Schneider et al., 2012) using the Skeletonize 3D plugin (Arganda-Carreras et al., 2010). The number of voxels composing the generated skeletons was computed in ImageJ using the Object Counter 3D plugin (Bolte and Cordelières, 2006). The length of analyzed biological structures (flagella and IFT trains) was calculated as the number of voxels constituting the skeletonized structure multiplied by the size of the voxel.

Distance measurement between IFT trains and individual doublets

IFT trains and doublets 3, 4, 7, and 8 were manually segmented on one flagellum to assess the distance between the IFT trains and the doublets. IFT train and doublet segmentations were skeletonized in ImageJ (Schneider et al., 2012) using the Skeletonize 3D plugin (Arganda-Carreras et al., 2010). We then computed in 3D the minimum distance between each voxel of the IFT train skeletons and the voxels of the doublet skeletons. This allowed to plot along the IFT train its distance with the various doublets in order to determine the closest one.

Statistical analyses

In absence of other indications, all errors correspond with the SD of the population. ANOVA tests were performed using the appropriate tool in Kaleidagraph (v4.5.2). Populations of IFT trains on doublets 4 and 7 were analyzed separately with the statistical analysis software R (R Core Team, 2014) using the normalMixEM algorithm of the Mixtools package (version 1.1.0; Benaglia et al., 2009) to check whether they were composed of subpopulations or not. This algorithm, based on expectation maximization, estimates the mean and SD values of Gaussian subpopulations and eventually converges to a solution if such subpopulations exist. Convergence was reached in 27 and 13 iterations for IFT trains on doublets 4 and 7, respectively.

SIM

Trypanosomes expressing the mNG::IFT81 fusion protein were spread on glass coverslips in medium, and SIM was performed on an LSM780 Elyra PS1 microscope (ZEISS) using 100×/1.46 NA oil Plan Apochromat objective and an electron-multiplying charge-coupled device (EMCCD) Andor IXon 887 1-K camera for the detection at Institut Pasteur. 15 images per plane per channel (five phases; three angles) were acquired to perform the SIM imaging. SIM imaging was processed with ZEN software (ZEISS). The SIMcheck plugin (Ball et al., 2015) in ImageJ (Schneider et al., 2012) was used to evaluate the acquisition and the processing parameters.

High-resolution imaging of IFT trafficking

The cell line expressing GFP::IFT52 and TdT::IFT81 was grown in standard conditions, and samples were mounted between glass and coverslip for observation on a custom-built microscope (Gustafsson, 2000; Gustafsson et al., 2008) based on an Axio-Observer D1 stand equipped with an UAPON100XOTIRF 1.49 NA objective (Olympus) and an Orca Flash 4.0 sCMOS camera (Hamamatsu Photonics). GFP fluorophores were excited with a 488-nm laser (500 mW; SAPPHIRE 488–500; Coherent) and detected through an adequate emission filter (BP 500–550 nm). The sequence contains a series of 300 images exposed for 20 ms each for a total duration of 17.7 s. Kymographs of individual paths of IFT were extracted using Fiji (ImageJ; Schindelin et al., 2012). The two IFT tracks were manually annotated as segmented lines on the temporal maximum-intensity projection of the sequence. These two lines were then used to reslice the sequence data, generating the kymographs that were analyzed using Icy (de Chaumont et al., 2012). Cell lines expressing mNG::IFT81 or GFP::DHC2.2 were grown in standard conditions, and samples were mounted between glass and quartz coverslips (cover glasses HI; 1787-996; ZEISS). For video acquisition, a spinning-disk confocal microscope (UltraView VOX; PerkinElmer) equipped with an oil-immersion objective Plan Apochromat 100×/1.57 NA oil HI differential interference contrast (ZEISS) was used. Videos were acquired using Volocity software with an EMCCD camera (C-9100; Hamamatsu Photonics) operating in streaming mode. The samples were kept at 27°C using a temperature-controlled chamber. Sequences of 30 s were acquired with an exposure time of 100 ms per frame. Kymographs were extracted and analyzed with Icy software (de Chaumont et al., 2012) using the plugin Kymograph Tracker 2 (Chenouard et al., 2010). The cells were positioned in the same orientation, with the posterior end on top and the flagellum on the left-hand side to define the left and right sides. The two traces left by IFT trains were manually defined as a region of interest using the temporal projection.

Dual-color acquisitions were performed with the cell line expressing mNG::IFT81 and TdT::DHC2.1 on a spinning-disk fluorescence microscope (UltraView VOX; PerkinElmer) equipped with confocal scanning head (CSU X1; Yokogawa) and a 100× 1.4 NA objective controlled by Volocity software. The CSU X1 incorporates a dichroic mirror that sends emitted light on two EMCCD cameras (ImageEM C9100; Hamamatsu Photonics) separately for wavelengths <550 nm and >550 nm. This allows for simultaneous dual-color imaging for red and green channels.

Immunofluorescence imaging

For paraformaldehyde–methanol fixation, cultured parasites were washed twice in SDM79 medium without serum and spread directly onto poly-L-lysine–coated slides (J2800AMMZ; Thermo Fisher Scientific). Cells were left for 10 min to settle before treatment with 1 vol 4% PFA solution in PBS, pH 7. After 5 min, slides were washed briefly in PBS before being fixed in pure methanol at a temperature of −20°C for 5 min, followed by a rehydration step in PBS for 15 min. For immunodetection, slides were incubated for 1 h at 37°C with the appropriate dilution of the first antibody in 0.1% BSA in PBS; mAb25 recognizes the axonemal protein TbSAXO1 (Pradel et al., 2006; Dacheux et al., 2012) and a monoclonal antibody against the IFT-B protein IFT172 (Absalon et al., 2008). After three consecutive 5-min washes in PBS, species and subclass-specific secondary antibodies coupled to the appropriate fluorochrome (Alexa Fluor 488; Cy3; Jackson ImmunoResearch Laboratories, Inc.) were diluted 1:400 in PBS containing 0.1% BSA and were applied for 1 h at 37°C. After washing in PBS as indicated above, cells were stained with a 1-µg/ml solution of the DNA dye DAPI (Roche) and mounted with the Slowfade antifade reagent (Invitrogen). Slides were immediately observed at room temperature with a DMI4000 microscope (Leica Microsystems) with a high-contrast Plan Apochromat 100× 1.4 NA objective (Leica Microsystems) using an ORCA-03G camera (Hamamatsu Photonics) with an EL6000 (Leica Microsystems) as a light excitation source. Image acquisition was performed using Micromanager software, and images were analyzed using ImageJ.

Western blotting

Cells were washed once in PBS. Laemmli loading buffer was added to the cells, and samples were boiled for 5 min. 20 µg protein was loaded into each lane of a Criterion XT Bis-Tris precast gel 4–12% (Bio-Rad Laboratories) for SDS-PAGE separation. XT-MOPS (1×) diluted in deionized water was used as a running buffer. Proteins were transferred onto nitrocellulose membranes using the Trans-Blot Turbo blotting system (25 V over 7 min; Bio-Rad Laboratories). The membrane was blocked with 5% skimmed milk for 1 h and then incubated with the monoclonal anti-mNG (32F6) primary antibody (ChromoTek) diluted 1:1,000 in 0.05% PBS–Tween-20 (PBST). As a loading control, the anti-PFR L13D6 monoclonal antibody (Kohl et al., 1999) diluted 1:25 was used. After primary antibody incubation, three washes of 5 min each were performed in 0.05% PBST followed by secondary antibody incubation. Anti-mouse secondary antibody was coupled to HRP and diluted to 1:20,000 in 0.05% PBST containing 0.1% milk, and then the membrane was incubated with this for 1 h. The Amersham ECL Western blotting detection reagent kit (GE Healthcare) was used for final detection of proteins on the membrane.

Online supplemental material

Fig. S1 shows that endogenous tagging of IFT81 with mNG provides a clean marker for monitoring IFT, with validation of the fusion protein by Western blotting, evidence of bidirectional IFT trafficking, and presence of two lines upon immunofluorescence assay using the paraformaldehyde–methanol protocol. Fig. S2 uses SIM imaging in live cells to reveal IFT trafficking on two separate sides of the axoneme, but the temporal resolution is not sufficient to visualize individual IFT trains. Fig. S3 illustrates bidirectional IFT trafficking on two sides of the axoneme in live trypanosomes expressing GFP::IFT52 showing still images at high resolution and kymograph analysis depicting the left and the right parts of the axoneme, with quantification of the frequency and speed of anterograde IFT trains. Fig. S4 shows the conversion of anterograde trains to retrograde trains at the distal tip, with magnification of a region of interest at this position. Kymograph analysis reveals the fragmentation of individual anterograde trains in smaller retrograde trains that remain on the same side of the axoneme. No evidence for transfer between the left and rights tracks could be observed. Video 1 shows the stack of original data of WT trypanosomes analyzed by FIB-SEM, where several cells are visible with all typical organelles including the flagellum. The position of three IFT trains present in the flagellum of the cell located in the center of the field is indicated. The same cell has been used for the segmentation analysis presented in Fig. 3. Video 2 is a reconstruction showing only individual flagella of the stack from Video 1 with IFT trains colored in red. The volume is then rotated in all dimensions to visualize the positioning of IFT trains. Video 3 shows live acquisition of a cell expressing mNG::IFT81 with robust bidirectional IFT. Video 4 is another live acquisition, this time by SIM of a cell expressing GFP::IFT52, showing the existence of two tracks for IFT trafficking. Videos 5 and 6 are live imaging by high-resolution microscopy using a 1.57 NA objective of a cell expressing mNG::IFT81 or using a 1.49 NA objective of a cell expressing GFP::IFT52, respectively. In both cases, bidirectional IFT trafficking is visible on two distinct lines. Similarly, Video 7 shows live imaging by high-resolution microscopy using a 1.57 NA objective of a cell expressing GFP::DHC2.2, where bidirectional IFT trafficking is visible on two distinct lines. Video 8 represents live imaging by conventional microscopy using a 1.40 NA objective of a cell expressing mNG::IFT81 (green) and TdT::DHC2.1 (magenta), where the two proteins colocalize on moving and standing trains. The video is completed with the kymograph analysis at Fig. 6 C. Video 9 shows live imaging by high-resolution microscopy using a 1.57 NA objective of a cell expressing mNG::IFT81. Focusing on the distal tip reveals the transit and turnaround of IFT material during the conversion of anterograde to retrograde trains. Videos 9 and 10 show live imaging by high-resolution microscopy of cells expressing GFP::IFT52 focusing on the distal tip to reveal the conversion of anterograde to retrograde trains. Video 10 is further analyzed in Fig. 7.

Acknowledgments

We thank Sylvie Perrot for the preparation of samples for FIB-SEM, Audrey Salles for the SIM acquisition performed on the Elyra SP1 system, Derrick Robinson (Bordeaux University, Bordeaux, France) for providing the Mab25 antibody, and Linda Kohl for critical reading of the manuscript. We thank Adrien Vuillaume for support and interest for this project. We are grateful to the Photonic Bioimaging and Ultrastructural Bioimaging facilities for access to their equipment. Some SIM and high-resolution microscopy work was performed at the Advanced Imaging Centre, Janelia Research Campus, jointly sponsored by the Howard Hughes Medical Institute and the Gordon and Betty Moore Foundation. We are grateful to Lin Shao for training and advice. The generosity and reactivity of Jim Morris are warmly acknowledged for having made this project feasible.

E. Bertiaux is supported by fellowships from French National Ministry for Research and Technology (doctoral school CDV515) and from La Fondation pour la Recherche Médicale (FDT20170436836). C. Fort was supported by fellowships from French National Ministry for Research and Technology (doctoral school CDV515) and from La Fondation pour la Recherche Médicale (FDT20150532023). This work is funded by Agence Nationale de la Recherche grants (11-BSV8-016 and 14-CE35-0009-01), by La Fondation pour la Recherche Médicale (Equipe FRM DEQ20150734356), and by a French Government Investissement d'Avenir program, Laboratoire d'Excellence "Integrative Biology of Emerging Infectious Diseases" (ANR-10-LABX-62-IBEID). We are also grateful for support for FESEM Zeiss Auriga and Elyra PS1 equipment from the French Government Program Investissements d'Avenir France BioImaging (N° ANR-10-INSB-04-01) and from a DIM-Malinf grant from the Région Ile-de-France. Travel to the Advanced Imaging Center at Janelia Farm Research Campus was supported by the Centre d'Innovation et Recherche Technologique of the Institut Pasteur.

The authors declare no competing financial interests.

Author contributions: E. Bertiaux segmented FIB-SEM data, conducted live-cell acquisition with the mNG::IFT81 or mNG::IFT81/TdT::DHC2.1 cell lines, extracted and analyzed the kymographs, performed the statistical analyses on IFT

trafficking, and contributed to figure preparation. A. Mallet acquired the FIB-SEM data, segmented them, and produced the corresponding videos as well as the analysis of kymographs and the acquisition of GFP::DHC2.2 images at high resolution. C. Fort prepared samples for FIB-SEM and carried out several segmentations, conducted the GFP::IFT52 acquisition, and performed kymograph analyses. T. Blisnick produced the cell line expressing GFP::IFT52, acquired the still images of mNG::IFT81 cell line, and assembled the figures. S. Bonnefoy developed the PFA/methanol fixation protocol and performed immunofluorescence data and acquisition. J. Jung characterized the mNG::IFT81-expressing cell line, performed several kymograph analyses, and contributed to setting up the high-NA microscopy in Institut Pasteur. M. Lemos acquired TEM images and was responsible for measurement of the diameter of the axoneme. S. Marco contributed to statistical analysis. S. Vaughan participated in the coordination of the 3D EM project. S. Trépout developed the scripts to perform the measurements of IFT trains (length and distance with the microtubule doublets) from FIB-SEM data and performed the corresponding statistical analysis to identify train subpopulations. J.-Y. Tinevez designed the live-imaging project performed at the Janelia Farm Research Campus and participated to the high-resolution video acquisition and quantification. P. Bastin conceived and coordinated the project and wrote the paper with contributions from all authors.

Submitted: 9 May 2018
Revised: 6 August 2018
Accepted: 21 September 2018

References

Absalon, S., T. Blisnick, L. Kohl, G. Toutirais, G. Doré, D. Julkowska, A. Tavenet, and P. Bastin. 2008. Intraflagellar transport and functional analysis of genes required for flagellum formation in trypanosomes. *Mol. Biol. Cell.* 19:929–944. https://doi.org/10.1091/mbc.e07-08-0749

Adhiambo, C., T. Blisnick, G. Toutirais, E. Delannoy, and P. Bastin. 2009. A novel function for the atypical small G protein Rab-like 5 in the assembly of the trypanosome flagellum. *J. Cell Sci.* 122:834–841. https://doi.org/10.1242/jcs.040444

Arganda-Carreras, I., R. Fernández-González, A. Muñoz-Barrutia, and C. Ortiz-De-Solorzano. 2010. 3D reconstruction of histological sections: Application to mammary gland tissue. *Microsc. Res. Tech.* 73:1019–1029. https://doi.org/10.1002/jemt.20829

Ball, G., J. Demmerle, R. Kaufmann, I. Davis, I.M. Dobbie, and L. Schermelleh. 2015. SIMcheck: a Toolbox for Successful Super-resolution Structured Illumination Microscopy. *Sci. Rep.* 5:15915. https://doi.org/10.1038/srep15915

Bastin, P., T. Sherwin, and K. Gull. 1998. Paraflagellar rod is vital for trypanosome motility. *Nature.* 391:548. https://doi.org/10.1038/35300

Beales, P.L., E. Bland, J.L. Tobin, C. Bacchelli, B. Tuysuz, J. Hill, S. Rix, C.G. Pearson, M. Kai, J. Hartley, et al. 2007. IFT80, which encodes a conserved intraflagellar transport protein, is mutated in Jeune asphyxiating thoracic dystrophy. *Nat. Genet.* 39:727–729. https://doi.org/10.1038/ng2038

Benaglia, T., D. Chauveau, D. Hunter, and D. Young. 2009. mixtools: An R Package for Analyzing Finite Mixture Models. *J. Stat. Softw.* 32:1–29. https://doi.org/10.18637/jss.v032.i06

Berriman, M., E. Ghedin, C. Hertz-Fowler, G. Blandin, H. Renauld, D.C. Bartholomeu, N.J. Lennard, E. Caler, N.E. Hamlin, B. Haas, et al. 2005. The genome of the African trypanosome Trypanosoma brucei. *Science.* 309:416–422. https://doi.org/10.1126/science.1112642

Besschetnova, T.Y., E. Kolpakova-Hart, Y. Guan, J. Zhou, B.R. Olsen, and J.V. Shah. 2010. Identification of signaling pathways regulating primary cilium length and flow-mediated adaptation. *Curr. Biol.* 20:182–187. https://doi.org/10.1016/j.cub.2009.11.072

Bhogaraju, S., L. Cajanek, C. Fort, T. Blisnick, K. Weber, M. Taschner, N. Mizuno, S. Lamla, P. Bastin, E.A. Nigg, and E. Lorentzen. 2013. Molecular basis of tubulin transport within the cilium by IFT74 and IFT81. *Science.* 341:1009–1012. https://doi.org/10.1126/science.1240985

Blisnick, T., J. Buisson, S. Absalon, A. Marie, N. Cayet, and P. Bastin. 2014. The intraflagellar transport dynein complex of trypanosomes is made of a heterodimer of dynein heavy chains and of light and intermediate chains of distinct functions. *Mol. Biol. Cell.* 25:2620–2633. https://doi.org/10.1091/mbc.e14-05-0961

Bolte, S., and F.P. Cordelières. 2006. A guided tour into subcellular colocalization analysis in light microscopy. *J. Microsc.* 224:213–232. https://doi.org/10.1111/j.1365-2818.2006.01706.x

Bonnefoy, S., C.M. Watson, K. Kernohan, M. Lemos, S. Hutchinson, J. Poulter, L. Crinnion, C. O'Callaghan, R. Hirst, A. Rutman, et al. 2018. Biallelic Mutations in LRRC56 encoding a protein associated with intraflagellar transport, cause mucociliary clearance and laterality defects. *bioRxiv.* (Preprint posted on March 27, 2018)https://doi.org/10.1101/288852

Bosch Grau, M., G. Gonzalez Curto, C. Rocha, M.M. Magiera, P. Marques Sousa, T. Giordano, N. Spassky, and C. Janke. 2013. Tubulin glycylases and glutamylases have distinct functions in stabilization and motility of ependymal cilia. *J. Cell Biol.* 202:441–451. https://doi.org/10.1083/jcb.201305041

Branche, C., L. Kohl, G. Toutirais, J. Buisson, J. Cosson, and P. Bastin. 2006. Conserved and specific functions of axoneme components in trypanosome motility. *J. Cell Sci.* 119:3443–3455. https://doi.org/10.1242/jcs.03078

Broadhead, R., H.R. Dawe, H. Farr, S. Griffiths, S.R. Hart, N. Portman, M.K. Shaw, M.L. Ginger, S.J. Gaskell, P.G. McKean, and K. Gull. 2006. Flagellar motility is required for the viability of the bloodstream trypanosome. *Nature.* 440:224–227. https://doi.org/10.1038/nature04541

Brooks, E.R., and J.B. Wallingford. 2012. Control of vertebrate intraflagellar transport by the planar cell polarity effector Fuz. *J. Cell Biol.* 198:37–45. https://doi.org/10.1083/jcb.201204072

Brun, R., and Schönenberger. 1979. Cultivation and in vitro cloning or procyclic culture forms of Trypanosoma brucei in a semi-defined medium. Short communication. *Acta Trop.* 36:289–292.

Buisson, J., N. Chenouard, T. Lagache, T. Blisnick, J.C. Olivo-Marin, and P. Bastin. 2013. Intraflagellar transport proteins cycle between the flagellum and its base. *J. Cell Sci.* 126:327–338. https://doi.org/10.1242/jcs.117069

Burkard, G., C.M. Fragoso, and I. Roditi. 2007. Highly efficient stable transformation of bloodstream forms of Trypanosoma brucei. *Mol. Biochem. Parasitol.* 153:220–223. https://doi.org/10.1016/j.molbiopara.2007.02.008

Casanova, M., F. de Monbrison, J. van Dijk, C. Janke, M. Pagès, and P. Bastien. 2015. Characterisation of polyglutamylases in trypanosomatids. *Int. J. Parasitol.* 45:121–132. https://doi.org/10.1016/j.ijpara.2014.09.005

Chan, K.Y., and K. Ersfeld. 2010. The role of the Kinesin-13 family protein TbKif13-2 in flagellar length control of Trypanosoma brucei. *Mol. Biochem. Parasitol.* 174:137–140. https://doi.org/10.1016/j.molbiopara.2010.08.001

Chenouard, N., J. Buisson, I. Bloch, P. Bastin, and J.C. Olivo-Marin. 2010. Curvelet analysis of kymograph for tracking bi-directional particles in flurescence microscopy images. *International Conference on Image Processing.* https://doi.org/10.1109/ICIP.2010.5652479

Chien, A., S.M. Shih, R. Bower, D. Tritschler, M.E. Porter, and A. Yildiz. 2017. Dynamics of the IFT machinery at the ciliary tip. *eLife.* 6:e28606. https://doi.org/10.7554/eLife.28606

Coutton, C., A.S. Vargas, A. Amiri-Yekta, Z.E. Kherraf, S.F. Ben Mustapha, P. Le Tanno, C. Wambergue-Legrand, T. Karaouzène, G. Martinez, S. Crouzy, et al. 2018. Mutations in CFAP43 and CFAP44 cause male infertility and flagellum defects in Trypanosoma and human. *Nat. Commun.* 9:686. https://doi.org/10.1038/s41467-017-02792-7

Craft, J.M., J.A. Harris, S. Hyman, P. Kner, and K.F. Lechtreck. 2015. Tubulin transport by IFT is upregulated during ciliary growth by a cilium-autonomous mechanism. *J. Cell Biol.* 208:223–237. https://doi.org/10.1083/jcb.201409036

Dacheux, D., N. Landrein, M. Thonnus, G. Gilbert, A. Sahin, H. Wodrich, D.R. Robinson, and M. Bonhivers. 2012. A MAP6-related protein is present in protozoa and is involved in flagellum motility. *PLoS One.* 7:e31344. https://doi.org/10.1371/journal.pone.0031344

Dagoneau, N., M. Goulet, D. Geneviève, Y. Sznajer, J. Martinovic, S. Smithson, C. Huber, G. Baujat, E. Flori, L. Tecco, et al. 2009. DYNC2H1 mutations cause asphyxiating thoracic dystrophy and short rib-polydactyly syndrome, type III. *Am. J. Hum. Genet.* 84:706–711. https://doi.org/10.1016/j.ajhg.2009.04.016

Dean, S., J.D. Sunter, and R.J. Wheeler. 2017. TrypTag.org: A Trypanosome Genome-wide Protein Localisation Resource. *Trends Parasitol.* 33:80–82. https://doi.org/10.1016/j.pt.2016.10.009

de Chaumont, F., S. Dallongeville, N. Chenouard, N. Hervé, S. Pop, T. Provoost, V. Meas-Yedid, P. Pankajakshan, T. Lecomte, Y. Le Montagner, et al. 2012. Icy: an open bioimage informatics platform for extended reproducible research. *Nat. Methods.* 9:690–696. https://doi.org/10.1038/nmeth.2075

Demonchy, R., T. Blisnick, C. Deprez, G. Toutirais, C. Loussert, W. Marande, P. Grellier, P. Bastin, and L. Kohl. 2009. Kinesin 9 family members perform separate functions in the trypanosome flagellum. *J. Cell Biol.* 187:615–622. https://doi.org/10.1083/jcb.200903139

Gadelha, C., B. Wickstead, P.G. McKean, and K. Gull. 2006. Basal body and flagellum mutants reveal a rotational constraint of the central pair microtubules in the axonemes of trypanosomes. *J. Cell Sci.* 119:2405–2413. https://doi.org/10.1242/jcs.02969

Gustafsson, M.G. 2000. Surpassing the lateral resolution limit by a factor of two using structured illumination microscopy. *J. Microsc.* 198:82–87. https://doi.org/10.1046/j.1365-2818.2000.00710.x

Gustafsson, M.G., L. Shao, P.M. Carlton, C.J. Wang, I.N. Golubovskaya, W.Z. Cande, D.A. Agard, and J.W. Sedat. 2008. Three-dimensional resolution doubling in wide-field fluorescence microscopy by structured illumination. *Biophys. J.* 94:4957–4970. https://doi.org/10.1529/biophysj.107.120345

Halbritter, J., A.A. Bizet, M. Schmidts, J.D. Porath, D.A. Braun, H.Y. Gee, A.M. McInerney-Leo, P. Krug, E. Filhol, E.E. Davis, et al. UK10K Consortium. 2013. Defects in the IFT-B component IFT172 cause Jeune and Mainzer-Saldino syndromes in humans. *Am. J. Hum. Genet.* 93:915–925. https://doi.org/10.1016/j.ajhg.2013.09.012

Heuser, T., C.F. Barber, J. Lin, J. Krell, M. Rebesco, M.E. Porter, and D. Nicastro. 2012. Cryoelectron tomography reveals doublet-specific structures and unique interactions in the I1 dynein. *Proc. Natl. Acad. Sci. USA.* 109:E2067–E2076. https://doi.org/10.1073/pnas.1120690109

Höög, J.L., S. Lacomble, C. Bouchet-Marquis, L. Briggs, K. Park, A. Hoenger, and K. Gull. 2016. 3D Architecture of the Trypanosoma brucei Flagella Connector, a Mobile Transmembrane Junction. *PLoS Negl. Trop. Dis.* 10:e0004312. https://doi.org/10.1371/journal.pntd.0004312

Huet, D., T. Blisnick, S. Perrot, and P. Bastin. 2014. The GTPase IFT27 is involved in both anterograde and retrograde intraflagellar transport. *eLife.* 3:e02419. https://doi.org/10.7554/eLife.02419

Hughes, L.C., K.S. Ralston, K.L. Hill, and Z.H. Zhou. 2012. Three-dimensional structure of the Trypanosome flagellum suggests that the paraflagellar rod functions as a biomechanical spring. *PLoS One.* 7:e25700. https://doi.org/10.1371/journal.pone.0025700

Hughes, L., S. Borrett, K. Towers, T. Starborg, and S. Vaughan. 2017. Patterns of organelle ontogeny through a cell cycle revealed by whole-cell reconstructions using 3D electron microscopy. *J. Cell Sci.* 130:637–647. https://doi.org/10.1242/jcs.198887

Imboden, M., N. Müller, A. Hemphill, R. Mattioli, and T. Seebeck. 1995. Repetitive proteins from the flagellar cytoskeleton of African trypanosomes are diagnostically useful antigens. *Parasitology.* 110:249–258. https://doi.org/10.1017/S0031182000080835

Iomini, C., V. Babaev-Khaimov, M. Sassaroli, and G. Piperno. 2001. Protein particles in Chlamydomonas flagella undergo a transport cycle consisting of four phases. *J. Cell Biol.* 153:13–24. https://doi.org/10.1083/jcb.153.1.13

Janke, C., K. Rogowski, D. Wloga, C. Regnard, A.V. Kajava, J.M. Strub, N. Temurak, J. van Dijk, D. Boucher, A. van Dorsselaer, et al. 2005. Tubulin polyglutamylase enzymes are members of the TTL domain protein family. *Science.* 308:1758–1762. https://doi.org/10.1126/science.1113010

Kelly, S., J. Reed, S. Kramer, L. Ellis, H. Webb, J. Sunter, J. Salje, N. Marinsek, K. Gull, B. Wickstead, and M. Carrington. 2007. Functional genomics in Trypanosoma brucei: a collection of vectors for the expression of tagged proteins from endogenous and ectopic gene loci. *Mol. Biochem. Parasitol.* 154:103–109. https://doi.org/10.1016/j.molbiopara.2007.03.012

Kizilyaprak, C., J. Daraspe, and B.M. Humbel. 2014. Focused ion beam scanning electron microscopy in biology. *J. Microsc.* 254:109–114. https://doi.org/10.1111/jmi.12127

Kohl, L., T. Sherwin, and K. Gull. 1999. Assembly of the paraflagellar rod and the flagellum attachment zone complex during the Trypanosoma brucei cell cycle. *J. Eukaryot. Microbiol.* 46:105–109. https://doi.org/10.1111/j.1550-7408.1999.tb04592.x

Konno, A., M. Setou, and K. Ikegami. 2012. Ciliary and flagellar structure and function--their regulations by posttranslational modifications of axonemal tubulin. *Int. Rev. Cell Mol. Biol.* 294:133–170. https://doi.org/10.1016/B978-0-12-394305-7.00003-3

Koyfman, A.Y., M.F. Schmid, L. Gheiratmand, C.J. Fu, H.A. Khant, D. Huang, C.Y. He, and W. Chiu. 2011. Structure of Trypanosoma brucei flagellum accounts for its bihelical motion. *Proc. Natl. Acad. Sci. USA.* 108:11105–11108. https://doi.org/10.1073/pnas.1103634108

Kozminski, K.G., K.A. Johnson, P. Forscher, and J.L. Rosenbaum. 1993. A motility in the eukaryotic flagellum unrelated to flagellar beating. *Proc. Natl. Acad. Sci. USA.* 90:5519–5523. https://doi.org/10.1073/pnas.90.12.5519

Kubo, T., J.M. Brown, K. Bellve, B. Craige, J.M. Craft, K. Fogarty, K.F. Lechtreck, and G.B. Witman. 2016. Together, the IFT81 and IFT74 N-termini form the main module for intraflagellar transport of tubulin. *J. Cell Sci.* 129:2106–2119. https://doi.org/10.1242/jcs.187120

Kuhns, S., and O.E. Blacque. 2016. Cilia Train Spotting. *Dev. Cell.* 37:395–396. https://doi.org/10.1016/j.devcel.2016.05.016

Lacomble, S., S. Vaughan, C. Gadelha, M.K. Morphew, M.K. Shaw, J.R. McIntosh, and K. Gull. 2009. Three-dimensional cellular architecture of the flagellar pocket and associated cytoskeleton in trypanosomes revealed by electron microscope tomography. *J. Cell Sci.* 122:1081–1090. https://doi.org/10.1242/jcs.045740

Lee, J.E., J.L. Silhavy, M.S. Zaki, J. Schroth, S.L. Bielas, S.E. Marsh, J. Olvera, F. Brancati, M. Iannicelli, K. Ikegami, et al. 2012. CEP41 is mutated in Joubert syndrome and is required for tubulin glutamylation at the cilium. *Nat. Genet.* 44:193–199. https://doi.org/10.1038/ng.1078

Li, D., L. Shao, B.C. Chen, X. Zhang, M. Zhang, B. Moses, D.E. Milkie, J.R. Beach, J.A. Hammer III, M. Pasham, et al. 2015. Extended-resolution structured illumination imaging of endocytic and cytoskeletal dynamics. *Science.* 349:aab3500. https://doi.org/10.1126/science.aab3500

Lin, J., T. Heuser, K. Song, X. Fu, and D. Nicastro. 2012. One of the nine doublet microtubules of eukaryotic flagella exhibits unique and partially conserved structures. *PLoS One.* 7:e46494. https://doi.org/10.1371/journal.pone.0046494

Mijalkovic, J., B. Prevo, F. Oswald, P. Mangeol, and E.J. Peterman. 2017. Ensemble and single-molecule dynamics of IFT dynein in Caenorhabditis elegans cilia. *Nat. Commun.* 8:14591. https://doi.org/10.1038/ncomms14591

Oberholzer, M., G. Langousis, H.T. Nguyen, E.A. Saada, M.M. Shimogawa, Z.O. Jonsson, S.M. Nguyen, J.A. Wohlschlegel, and K.L. Hill. 2011. Independent analysis of the flagellum surface and matrix proteomes provides insight into flagellum signaling in mammalian-infectious Trypanosoma brucei. *Mol. Cell. Proteomics.* https://doi.org/10.1074/mcp.M111.010538

Pathak, N., C.A. Austin, and I.A. Drummond. 2011. Tubulin tyrosine ligase-like genes ttll3 and ttll6 maintain zebrafish cilia structure and motility. *J. Biol. Chem.* 286:11685–11695. https://doi.org/10.1074/jbc.M110.209817

Perrault, I., S. Saunier, S. Hanein, E. Filhol, A.A. Bizet, F. Collins, M.A. Salih, S. Gerber, N. Delphin, K. Bigot, et al. 2012. Mainzer-Saldino syndrome is a ciliopathy caused by IFT140 mutations. *Am. J. Hum. Genet.* 90:864–870. https://doi.org/10.1016/j.ajhg.2012.03.006

Pigino, G., S. Geimer, S. Lanzavecchia, E. Paccagnini, F. Cantele, D.R. Diener, J.L. Rosenbaum, and P. Lupetti. 2009. Electron-tomographic analysis of intraflagellar transport particle trains in situ. *J. Cell Biol.* 187:135–148. https://doi.org/10.1083/jcb.200905103

Pradel, L.C., M. Bonhivers, N. Landrein, and D.R. Robinson. 2006. NIMA-related kinase TbNRKC is involved in basal body separation in Trypanosoma brucei. *J. Cell Sci.* 119:1852–1863. https://doi.org/10.1242/jcs.02900

Prevo, B., P. Mangeol, F. Oswald, J.M. Scholey, and E.J. Peterman. 2015. Functional differentiation of cooperating kinesin-2 motors orchestrates cargo import and transport in C. elegans cilia. *Nat. Cell Biol.* 17:1536–1545. https://doi.org/10.1038/ncb3263

Prevo, B., J.M. Scholey, and E.J.G. Peterman. 2017. Intraflagellar transport: mechanisms of motor action, cooperation, and cargo delivery. *FEBS J.* 284:2905–2931. https://doi.org/10.1111/febs.14068

Ralston, K.S., A.G. Lerner, D.R. Diener, and K.L. Hill. 2006. Flagellar motility contributes to cytokinesis in Trypanosoma brucei and is modulated by an evolutionarily conserved dynein regulatory system. *Eukaryot. Cell.* 5:696–711. https://doi.org/10.1128/EC.5.4.696-711.2006

R Core Team. 2014. R: A language and environment for statistical computing. R Foundation for Statistical Computing, Vienna, Austria. http://www.R-project.org/. See information at https://stat.ethz.ch/pipermail/r-help/2014-October/422975.html

Ringo, D.L. 1967. Flagellar motion and fine structure of the flagellar apparatus in Chlamydomonas. *J. Cell Biol.* 33:543–571. https://doi.org/10.1083/jcb.33.3.543

Rogowski, K., F. Juge, J. van Dijk, D. Wloga, J.M. Strub, N. Levilliers, D. Thomas, M.H. Bré, A. Van Dorsselaer, J. Gaertig, and C. Janke. 2009. Evolutionary divergence of enzymatic mechanisms for posttranslational polyglycylation. *Cell.* 137:1076–1087. https://doi.org/10.1016/j.cell.2009.05.020

Rompolas, P., L.B. Pedersen, R.S. Patel-King, and S.M. King. 2007. Chlamydomonas FAP133 is a dynein intermediate chain associated with the retrograde intraflagellar transport motor. *J. Cell Sci.* 120:3653–3665. https://doi.org/10.1242/jcs.012773

Santrich, C., L. Moore, T. Sherwin, P. Bastin, C. Brokaw, K. Gull, and J.H. LeBowitz. 1997. A motility function for the paraflagellar rod of Leishmania parasites revealed by PFR-2 gene knockouts. *Mol. Biochem. Parasitol.* 90:95–109. https://doi.org/10.1016/S0166-6851(97)00149-7

Schindelin, J., I. Arganda-Carreras, E. Frise, V. Kaynig, M. Longair, T. Pietzsch, S. Preibisch, C. Rueden, S. Saalfeld, B. Schmid, et al. 2012. Fiji: an open-source platform for biological-image analysis. *Nat. Methods.* 9:676–682. https://doi.org/10.1038/nmeth.2019

Schneider, A., U. Plessmann, and K. Weber. 1997. Subpellicular and flagellar microtubules of Trypanosoma brucei are extensively glutamylated. *J. Cell Sci.* 110:431–437.

Schneider, C.A., W.S. Rasband, and K.W. Eliceiri. 2012. NIH Image to ImageJ: 25 years of image analysis. *Nat. Methods.* 9:671–675. https://doi.org/10.1038/nmeth.2089

Shaner, N.C., G.G. Lambert, A. Chammas, Y. Ni, P.J. Cranfill, M.A. Baird, B.R. Sell, J.R. Allen, R.N. Day, M. Israelsson, et al. 2013. A bright monomeric green fluorescent protein derived from Branchiostoma lanceolatum. *Nat. Methods.* 10:407–409. https://doi.org/10.1038/nmeth.2413

Sherwin, T., and K. Gull. 1989. The cell division cycle of Trypanosoma brucei brucei: timing of event markers and cytoskeletal modulations. *Philos. Trans. R. Soc. Lond. B Biol. Sci.* 323:573–588. https://doi.org/10.1098/rstb.1989.0037

Sirajuddin, M., L.M. Rice, and R.D. Vale. 2014. Regulation of microtubule motors by tubulin isotypes and post-translational modifications. *Nat. Cell Biol.* 16:335–344. https://doi.org/10.1038/ncb2920

Snow, J.J., G. Ou, A.L. Gunnarson, M.R. Walker, H.M. Zhou, I. Brust-Mascher, and J.M. Scholey. 2004. Two anterograde intraflagellar transport motors cooperate to build sensory cilia on C. elegans neurons. *Nat. Cell Biol.* 6:1109–1113. https://doi.org/10.1038/ncb1186

Stepanek, L., and G. Pigino. 2016. Microtubule doublets are double-track railways for intraflagellar transport trains. *Science.* 352:721–724. https://doi.org/10.1126/science.aaf4594

Subota, I., D. Julkowska, L. Vincensini, N. Reeg, J. Buisson, T. Blisnick, D. Huet, S. Perrot, J. Santi-Rocca, M. Duchateau, et al. 2014. Proteomic analysis of intact flagella of procyclic Trypanosoma brucei cells identifies novel flagellar proteins with unique sub-localization and dynamics. *Mol. Cell. Proteomics.* 13:1769–1786. https://doi.org/10.1074/mcp.M113.033357

Taschner, M., and E. Lorentzen. 2016. The Intraflagellar Transport Machinery. *Cold Spring Harb. Perspect. Biol.* 8:a028092. https://doi.org/10.1101/cshperspect.a028092

Tetley, L., and K. Vickerman. 1985. Differentiation in Trypanosoma brucei: host-parasite cell junctions and their persistence during acquisition of the variable antigen coat. *J. Cell Sci.* 74:1–19.

van Dijk, J., K. Rogowski, J. Miro, B. Lacroix, B. Eddé, and C. Janke. 2007. A targeted multienzyme mechanism for selective microtubule polyglutamylation. *Mol. Cell.* 26:437–448. https://doi.org/10.1016/j.molcel.2007.04.012

Vannuccini, E., E. Paccagnini, F. Cantele, M. Gentile, D. Dini, F. Fino, D. Diener, C. Mencarelli, and P. Lupetti. 2016. Two classes of short intraflagellar transport train with different 3D structures are present in Chlamydomonas flagella. *J. Cell Sci.* 129:2064–2074. https://doi.org/10.1242/jcs.183244

Wheeler, R.J., E. Gluenz, and K. Gull. 2015. Basal body multipotency and axonemal remodelling are two pathways to a 9+0 flagellum. *Nat. Commun.* 6:8964. https://doi.org/10.1038/ncomms9964

Williams, C.L., J.C. McIntyre, S.R. Norris, P.M. Jenkins, L. Zhang, Q. Pei, K. Verhey, and J.R. Martens. 2014. Direct evidence for BBSome-associated intraflagellar transport reveals distinct properties of native mammalian cilia. *Nat. Commun.* 5:5813. https://doi.org/10.1038/ncomms6813

Wingfield, J.L., I. Mengoni, H. Bomberger, Y.Y. Jiang, J.D. Walsh, J.M. Brown, T. Picariello, D.A. Cochran, B. Zhu, J. Pan, et al. 2017. IFT trains in different stages of assembly queue at the ciliary base for consecutive release into the cilium. *eLife.* 6:e26609. https://doi.org/10.7554/eLife.26609

Wirtz, E., and C. Clayton. 1995. Inducible gene expression in trypanosomes mediated by a prokaryotic repressor. *Science.* 268:1179–1183. https://doi.org/10.1126/science.7761835

Wloga, D., D.M. Webster, K. Rogowski, M.H. Bré, N. Levilliers, M. Jerka-Dziadosz, C. Janke, S.T. Dougan, and J. Gaertig. 2009. TTLL3 Is a tubulin glycine ligase that regulates the assembly of cilia. *Dev. Cell.* 16:867–876. https://doi.org/10.1016/j.devcel.2009.04.008